Article

Rational Design and Evaluation of Photoactive Molecularly Imprinted Nanoparticles for Tetracycline Degradation Under Visible Light

Yadiris García, Joao Aguilar, Laura Polania, Yorley Duarte, Börje Sellergren, and Verónica A. Jiménez*

Read Online

ACCESS | Metrics & More | Article Recommendations | SI Supporting Information

ABSTRACT: This work presents the use of photoactive molecularly imprinted nanoparticles (MINs) to promote antibiotic degradation under visible light irradiation. Prototype MINs for the model antibiotic tetracycline (TC) were developed using molecular dynamics simulations to predict the TC-binding capacity of seven pre-polymerization mixtures. The studied formulations contained varying proportions of functional monomers with diverse physicochemical profiles, namely N-isopropylacrylamide (NIPAM), N-tert-butylacrylamide (TBAM), acrylic acid (AA), and (N-(3-aminopropyl)methacrylamide hydrochloride) (APMA) and a constant ratio of the cross-linker N,N'-methylene-bis-acrylamide (BIS). Two monomer formulations showed markedly higher TC-binding capacities based on template−monomer interaction energies. These mixtures were used to synthesize photoactive MINs by high-dilution radical polymerization, followed by the EDC/NHS conjugation with the organic photosensitizer toluidine blue. MINs showed higher TC-binding capacities than non-imprinted nanoparticles (nINs) of identical composition. MINs and nINs exhibited photodynamic activity under visible light irradiation, as confirmed by singlet oxygen generation experiments. TC degradation was evaluated in 50 μmol L^{-1} solutions placed in microplate wells containing immobilized nanoparticles and irradiated with white LED light (150 W m^{-2}) for 1 h at room temperature. Degradation followed pseudo-zero-order kinetics with accelerated profiles in MIN-containing wells. Our findings suggest a key role of molecularly imprinted cavities in bringing TC closer to the photosensitizing moieties, minimizing the loss of oxidative potential due to reactive oxygen species diffusion. This degradation strategy can potentially extend to any organic pollutants for which MINs can be synthesized and opens valuable opportunities for exploring novel applications for molecularly imprinted materials.
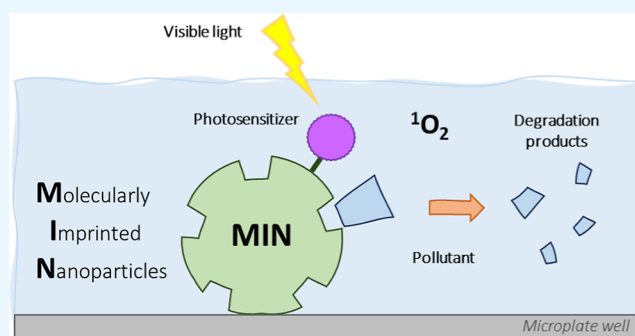
1. INTRODUCTION

Antibiotic pollution is a global threat to human, animal, and environmental health due to the persistence and progressive accumulation in water bodies, soil, and ecosystems world-wide.[1,2] Tetracycline (TC) is one of the most commonly used antibiotics due to its broad-spectrum activity, low price, high efficacy, and versatility for human and veterinary applications (Figure 1A). Yet, its poor degradability constitutes a significant source of antibiotic pollution. Several methods for TC removal have been developed, including biological and chemical degradation and physical removal strategies.[3,4] Photochemical degradation is an advantageous strategy that uses UV radiation and photosensitizing materials to generate reactive oxygen species (ROS) that cleave TC into smaller fragments with less harmful or nonhazardous effects.[5−9] TC does not degrade under visible light, which is a relevant goal for developing cheaper and milder experimental strategies for TC removal. To contribute to this challenge, we present a novel strategy for TC degradation based on photoactive molecularly imprinted nanoparticles (MINs) (Figure 1B). This approach takes advantage of the specific binding capacity of molecularly imprinted materials and the photodynamic activity conferred by a surface-conjugated photosensitizer to promote the photochemical degradation of a target compound near the nanomaterial surface. To the best of our knowledge, this is the first time this hypothesis is tested, thereby opening valuable opportunities for MIN-based applications.
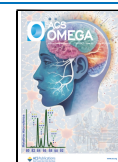
Molecularly imprinted materials are synthetic cross-linked polymers capable of recognizing a molecular target or template through specific binding sites created during the copolymerization of functional monomers and a cross-linker around the template. The target compound is removed at the end of the process, leaving complementary cavities in size and shape.
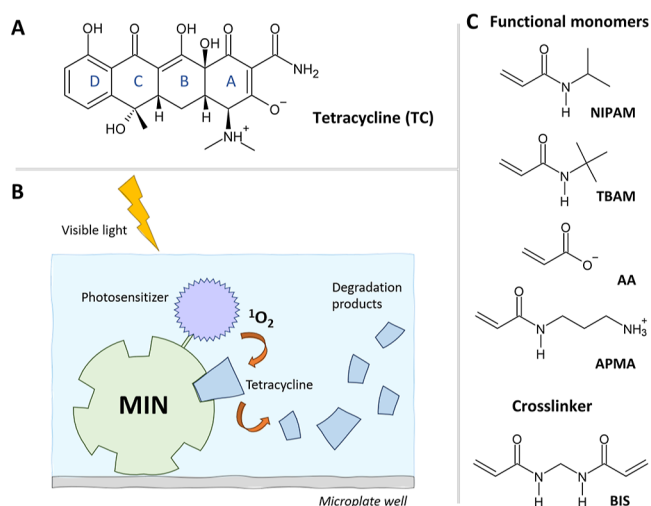
Figure 1. (A) Structure of TC. (B) Schematic representation of the proposed strategy for the degradation of TC in aqueous solution by visible light irradiation via photoactive MINs. (C) Structures of the functional monomers *N*-isopropylacrylamide (NIPAM), *N*-tert-butylacrylamide (TBAM), acrylic acid (AA), and (*N*-(3-aminopropyl)methacrylamide hydrochloride) (APMA), and the cross-linker *N,N′*-methylene-bis-acrylamide (BIS).

Computational modeling methods have emerged as relevant tools to assist the selection of functional monomers and their appropriate ratios for the synthesis of molecularly imprinted materials.[32,33] Major applications in this regard arise from molecular dynamics (MD) simulations addressing the structural and energetic aspects responsible for the preorganization of functional monomers around the template, which are critical for the generation of molecularly imprinted cavities during the subsequent polymerization step. Short or in vacuum MD simulations have been used to evaluate monomer arrangements in pre-polymerization complexes for diverse molecular targets, such as creatinine,[34] microcystin-LR,[35] carbamate moieties,[36] melamine,[37] acetamide,[38] 17-*β*-estradiol,[39,40] and norfloxacin,[41] among others. Recently, more realistic settings for MD simulations, including explicit solvent molecules, counterions, and multiple monomer compositions, have been applied to address the recognition of various biomolecular targets, including monosaccharides,[42] hormones,[43] and proteins.[44,45] These advances raise the opportunity of using MD simulations to optimize the design of molecularly imprinted materials for TC recognition, using more complex and diverse monomer mixtures than those so far reported experimentally to achieve binding sites with an enhanced affinity toward the target.

To that aim, we conducted MD simulations in seven prepolymerization mixtures for TC recognition containing different proportions of functional monomers with diverse physicochemical profiles, namely *N*-isopropylacrylamide (NIPAM), *N*-tert-butylacrylamide (TBAM), acrylic acid (AA), and (*N*-(3-aminopropyl)methacrylamide hydrochloride) (APMA), and a constant ratio of the cross-linker *N,N′*-methylene-bis-acrylamide (BIS) (Figure 1C). Two monomer mixtures were selected based on template−monomer interaction energies calculated under the linear interaction energy (LIE) approach. The chosen compositions were used to synthesize MINs for TC binding via radical polymerization in an aqueous medium. MINs were surface-modified with the well-known photosensitizer toluidine blue via EDC/NHS covalent coupling and characterized by dynamic light scattering (DLS) and singlet oxygen generation experiments. The prepared materials were immobilized onto polystyrene microplate wells by physical adsorption and subjected to rebinding assays that confirmed their higher TC binding capacity over analogous non-imprinted nanoparticles (nINs),

Molecularly imprinted polymers have gained increasing interest in sensing, separation, purification, and drug delivery due to their high physical and chemical stability, low cost, functional robustness, and ability to target structurally diverse compounds, including TC and other antibiotics.[10−23] Molecularly imprinted materials aimed at TC removal or detection have been obtained using acrylic or methacrylic acid as single functional monomers[15,24−29] or binary mixtures of acrylic or methacrylic acid with acrylamide or vinylpyridine monomers[29,30] in combination with common cross-linkers like ethylene glycol dimethacrylate, epichlorohydrin or TRIM. Recently, an aptamer-cyclodextrin-based molecularly imprinted polymer cross-linked with *N,N′*-methylene bis(acrylamide) (MBA) was developed for tetracyclin separation.[31] An unexplored aspect in this regard is customizing more complex monomer mixtures to maximize the recognition potential toward TC, which is relevant for developing molecularly imprinted materials with high affinity and selectivity.

Table 1. Composition of the Pre-Polymerization Systems Studied by MD Simulations[a]

mixture	mixture components											
	100 monomers + cross-linkers						200 monomers + cross-linkers					
	AA	NIPAM	TBAM	APMA	BIS	water	AA	NIPAM	TBAM	APMA	BIS	water
m0	100	0	0	0	5	2.91×10^4	200	0	0	0	10	3.53×10^4
m1	0	40	40	15	5	2.35×10^4	0	80	80	30	10	2.45×10^4
m2	23	25	25	22	5	2.26×10^4	45	50	50	45	10	2.18×10^4
m3	15	40	40	0	5	2.30×10^4	30	80	80	0	10	2.21×10^4
m4	40	8	8	39	5	2.25×10^4	80	15	15	80	10	2.20×10^4
m5	15	20	60	0	5	2.28×10^4	30	40	120	0	10	2.37×10^4
m6	15	60	20	0	5	2.29×10^4	30	120	40	0	10	2.17×10^4
m7	0	48	47	0	5	2.26×10^4	0	95	95	0	10	2.13×10^4

[a]Each system comprises one unit of the template (TC) surrounded by 100 or 200 units of monomers plus crosslinkers and a suitable number of Na+ or Cl− counterions to achieve charge neutrality. The number of water molecules is roughly similar among all systems. Monomer acronyms are AA, acrylic acid; NIPAM, *N*-isopropylacrylamide; TBAm, *N*-tert-butylacrylamide; APMA, *N*-(3-aminopropyl)methacrylamide hydrochloride; BIS, *N,N′*-methylene-bis-acrylamide.

thus supporting the validity of our computational predictions. The immobilized MINs were used in the photochemical degradation of TC in aqueous solution under visible light irradiation. TC degrades faster in MIN-containing wells, confirming our working hypothesis.

2. MATERIALS AND METHODS

2.1. Reagents. TC, N-isopropylacrylamide (NIPAM), N-*tert*-butylacrylamide (TBAm), N,N'-methylene-bis-acrylamide (BIS), acrylic acid (AA), N-(3-aminopropyl)methacrylamide hydrochloride (APMA), ammonium persulfate (APS), N,N,N',N'-tetramethylethylenediamine (TEMED), toluidine blue O (TBO). N-Hydroxysuccinimide (NHS), 1-ethyl-3-(3-dimethylaminopropyl) carbodiimide HCl (EDC). Dialysis bags (Merck Millipore), Singlet Oxygen Sensor Green (SOSG) (Invitrogen). Reagents and solvents were analytical or HPLC grade and used without further purification if not otherwise specified.

2.2. Molecular Dynamics Simulations. Atomic coordinates for the monomers NIPAM, TBAm, AA, APMA, and the cross-linker BIS were obtained from geometry optimization calculations at B3LYP/6-31G(d) level using the Gaussian16 software.[46] Coordinates for TC were obtained from the crystallographic complex of the TtgR protein in complex with TC with PDB code 2UXO.[47] The total charge of each species was set to their preferred protonation states at pH 7.0. TC was modeled as a zwitterion in which the secondary amine is protonated and the phenol group of ring A is deprotonated (Figure 1A). Simulation parameters consistent with the GAFF2 force field with AM1-BCC charges were obtained for the template, monomers and cross-linker using the Antechamber module of AmberTools20.[48,49] Seven prepolymerization mixtures containing three or four functional monomers in varying proportions plus a constant ratio of the cross-linker BIS were assembled using the Packmol software (Table 1). An eighth system containing AA as a single functional monomer was added as a control. Each mixture was simulated at two concentration conditions by keeping their monomer proportions and varying the total number of monomers plus cross-linker from 100 to 200 units. Mixtures were neutralized with the proper number of counterions to achieve charge neutrality and solvated with explicit OPC water molecules with a 5 Å solvation layer, resulting in $85 \times 85 \times 85$ Å^3 systems. MD simulations were carried out using the pmemd.CUDA software in the AMBER20 package.[50,51] The simulation protocol consisted of: (a) 1500 steepest descent minimization plus 3500 conjugate gradient minimization steps for water relaxation, (b) 1500 steepest descent minimization steps followed by 6500 conjugate gradient minimization steps for the entire system, (c) 500 ps of progressive NVT heating from 0 to 300 K, (d) 10 ns of NPT equilibrium at 300 K to ensure density equilibration, (e) 20 ns of NPT equilibrium at 300 K, and finally (f) 300 ns of NPT production dynamics at 300 K and 1 bar from which production data were collected. MD simulations used a 10 Å cutoff for non-bonded energy terms, bonds involving hydrogen atoms were constrained using the SHAKE algorithm, and long-range electrostatics were treated using the Particle-Mesh Ewald approach. Trajectory analysis was carried out using the CPPTRAJ[52] and VMD[53] software.

2.3. MINs Synthesis. Two pre-polymerization mixtures were experimentally assayed to obtain molecularly imprinted (MINs) and nINs. Polymerization was carried out by mixing 0.02 mmol of TC with the appropriate quantities of functional

monomers (NIPAM, TBAm, AA, APM) and cross-linker (BIS) in 20 mL of ultrapure water, as detailed in Table 2. Parallel

Table 2. Experimental Composition of the Monomer Mixtures Used to Synthesize MINs and nINs for TC Recognition

material name	mixture composition (mmol)					
	AA	NIPAM	TBAM	APMA	BIS	TC
MIN3	0.0510	0.136	0.136	0.000	0.0170	0.02
MIN4	0.136	0.0255	0.0255	0.136	0.0170	0.02
nIN3	0.0510	0.136	0.136	0.000	0.0170	0.02
nIN4	0.136	0.0255	0.0255	0.136	0.0170	0.02

mixtures were prepared in TC-free solutions for nINs synthesis. Mixtures were stirred at room temperature for 1.0 h in glass vials and purged with an N$_2$ stream for 20 min. Radical polymerization began after adding 0.100 mmol of APS and 0.150 mmol of TEMED dissolved in ultrapure water. The reaction proceeded for 12 h under shaking at 40.0 °C. Then, 1.0 mmol of EDC and 1.0 mmol of NHS were added to each solution and stirred for 15 min, followed by toluidine blue addition to a final concentration of 2.5 mmol/L. Systems were stirred in the dark for 12 h and thoroughly dialyzed against ultrapure water to remove TC and unreacted toluidine blue from the obtained polymers (MINs and nINs). TC and toluidine blue removal were monitored by measuring the decrease in absorbance at 360 and 564 nm, respectively.

2.4. DLS Experiments. DLS measurements were conducted in a Zetasizer Advance Lab device by Malvern Analytical (Malvern, UK), equipped with an avalanche photodiode detector and a He−Ne laser with a 4 mW output at a wavelength of 633 nm. Polymer dispersions (MINs or nINs) at 1.0 mg mL^{-1} were sonicated at 40 kHz for 5 min and filtered with a 0.45 μm syringe filter to 4.0 mL disposable polystyrene cuvettes. Size measurements were conducted at 25 °C with a fixed scattering angle of 90°. The zeta potential was determined with the same equipment, using disposable DTS1070 folded capillary cells in the M3-PALS analysis with a constant current zeta mode. Experiments were conducted in triplicate (n = 3), with each replicate representing an average of 25 and 100 measurements for DLS and zeta potential, respectively.

2.5. TC Rebinding Assays. 200 μL of polymer dispersions (MINs and nINs) at 0.1 mg mL^{-1} concentration were placed onto clean 12-well polystyrene plates and dried under constant stirring at 37 °C in the dark. Treated wells were washed twice with 100 μL of ultrapure water and 100 μL of ethanol and filled with 200 μL aqueous solutions of TC 50 μmol L^{-1} under constant stirring in the dark at room temperature for 12 h. Parallel experiments were conducted in nontreated (empty) wells under identical conditions. Supernatant samples of 100 μL were taken from the treated and nontreated wells and transferred to a clean 96-well microplate for UV−vis experiments using a POLARstar Omega microplate reader (BMG Labtech, Germany). The remaining concentration of TC in the supernatants was measured from the absorbance at 360 nm data and a previously validated calibration curve data. Experiments were carried out in triplicate.

2.6. Singlet Oxygen Generation Experiments. 100 μL of polymer dispersions (MINs and nINs) at 0.1 mg mL^{-1} concentration were placed onto clean black flat-bottom 96-well plates and dried overnight at 37 °C. Treated wells were washed

twice with 100 μL of ultrapure water and 100 μL of ethanol and filled with 100 μL of an aqueous solution of the commercial Singlet Oxygen Singlet Green (SOSG) sensor (5 μmol L^{-1}). Fluorescence intensity at t = 0 min was measured at an excitation wavelength of 485 nm and an emission wavelength of 520 nm. Microplate wells were then irradiated for 30 min using a cold white LED lamp with maximum emissions wavelengths of 450 and 550 nm and a radiation intensity of 150 W m^{-2}. Fluorescence intensity was measured at 5 min intervals during the irradiation period at identical excitation/emission wavelengths. Parallel experiments were conducted using non-treated wells as control systems. All experiments were carried out in triplicate.

2.7. TC Photodegradation Assays. 100 μL of polymer dispersions (MINs and nINs) at 0.1 mg mL^{-1} concentration were placed onto clean transparent 96-well plates and dried overnight at 37 °C. Treated wells were washed twice with 100 μL of ultrapure water and 100 μL of ethanol and filled with 100 μL of TC 50 μmol L^{-1} in ultrapure water. Parallel experiments were conducted in nontreated wells for control purposes. Microplate wells were irradiated for 60 min using a white light LED lamp with a radiation intensity of 150 W m^{-2} (Figure S1). Absorbance spectra were monitored every 15 min to evaluate the TC degradation. Additional TC photo-degradation assays were conducted using TC 50 μmol L^{-1} solutions prepared in ultrapure water supplemented with oxygen nanobubbles (ONBs). ONB-supplemented water was produced with a NanoBubble Generator (Holly Technology, China) that generates nanodiameter bubbles through a high-pressure rotary flow transient release technology. ONBs were produced for 20 min at 10 °C using a 4 L/min gas flow. The nanobubble solution was stabilized for 10 min before use.

3. RESULTS

This work reports the rational design and experimental evaluation of photoactive MINs to mediate the photochemical degradation of TC in aqueous solution by visible light irradiation. The rational design step aimed at setting the optimal composition of the monomer mixture to achieve molecularly imprinted cavities with high binding capacity toward the target compound TC. To that aim, we conducted molecular dynamics (MD) simulations in pre-polymerization mixtures differing in monomer composition to identify the monomer ratios that maximize the noncovalent interactions with the template. These interactions will account for the stability of pre-polymerization complexes in each formulation, which are critical for the success of molecular imprinting.[54,55]

3.1. MD Simulations on Prepolymerization Mixtures. MD simulations were carried out to evaluate the TC-binding capacity of seven pre-polymerization mixtures (**m1**−**m7**) containing variable monomer types and ratios (Table 1). A control system (**m0**), composed of acrylic acid (AA) as the only functional monomer, was included in our study to compare the TC-binding performance of **m1**−**m7** with a formulation that has been used in the literature for the synthesis of molecularly imprinted polymers for TC recognition.[15,24−29] Two monomer concentration conditions were simulated for each formulation. To this end, we assembled mixtures with either 100 (low monomer concentration) or 200 (high monomer concentration) monomer units surrounding one template, keeping a constant volume (Figure 2). The mixtures were completed by adding 5 or 10 cross-linker units to low monomer concentration and high monomer concen-
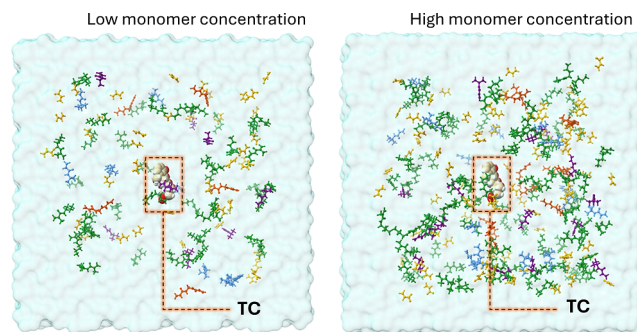

Figure 2. Representative input structures of the simulated pre-polymerization mixtures in low and high monomer concentration conditions. The systems were assembled by placing one TC unit at the center of a cubic box and surrounding it with either 100 or 200 monomer units at ratios corresponding to the monomer formulations detailed in Table 1. Systems were added with a constant cross-linker ratio (BIS, orange) and solvated with explicit water molecules. Functional monomers in the mixtures are depicted in different colors (NIPAM, purple; TBAM, light blue; AA, yellow; APMA, green).

tration mixtures, respectively. The functional monomers selected to conduct our study, namely N-isopropylacrylamide (NIPAM), N-tert-butylacrylamide (TBAM), acrylic acid (AA), and (N-(3-aminopropyl)methacrylamide hydrochloride) (APMA), have different physicochemical profiles and rich functionality for noncovalent interactions (Figure 1C). NIPAM, TBAM, and APMA are polar monomers with hydrogen bonding and van der Waals interaction capacities through their amide and aliphatic functionalities, respectively. AA and APMA possess charged moieties that can engage in electrostatic interactions with the pre-polymerization mixture and increase the hydrophilicity of the synthesized materials. The aliphatic segments in NIPAM, TBAM and APMA will reduce the polarity of the mixture and contribute to hydrophobic interactions within the pre-polymerization systems. Finally, the positively charged 3-aminopropyl moiety of APMA can form cation−π interactions with the aromatic rings of TC. This functional diversity will translate into a delicate interplay between monomer−monomer and template−monomer interactions that will determine the stability of the pre-polymerization complexes in different formulations. MD simulations will provide molecular-level insight into this interplay by describing the structural organization of monomer mixtures around the template and the energetics of template−monomer interactions.

MD trajectories were sampled for 300 ns (600 frames) in the production phase to estimate the strength of template−monomer interactions under the LIE approach. LIE energies were calculated for each frame as the sum of the noncovalent interactions between all atom pairs in the template and the surrounding monomers, expressed as electrostatic (E_{elec}) and van der Waals (E_{vdV}) contributions. Mean values for LIE energy terms (E_{vdV}, E_{elec} and E_{total}) and their corresponding standard deviations at low and high monomer concentration conditions are reported in Figure 3. For E_{vdV} terms, the mixtures **m1**−**m7** showed mean interaction energies close to −4 kcal/mol (low monomer concentration) and −7 kcal/mol (high monomer concentration) with minimum variations among formulations but much lower values than the control system **m0** (−1 to −2 kcal/mol). The strengthening of the E_{vdV} terms in **m1**−**m7** over **m0** arises from the presence of aliphatic moieties in NIPAM, TBAM and APMA, which can
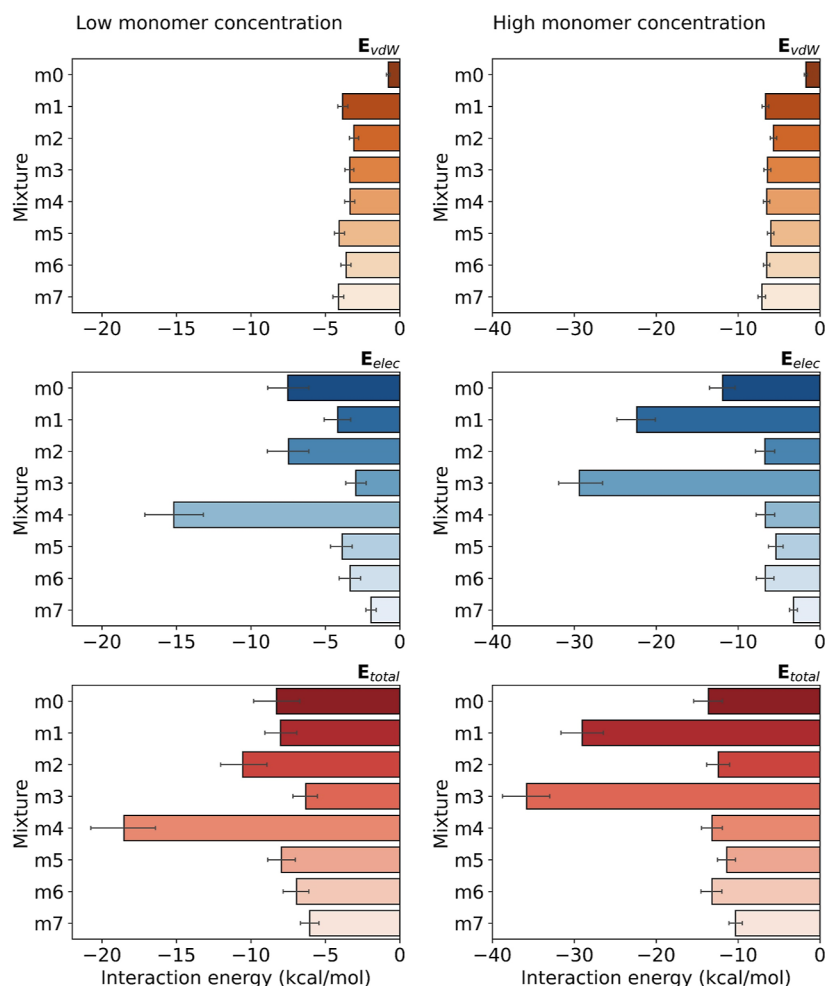
Figure 3. Template-monomer interaction energies (kcal/mol) for seven prepolymerization mixtures (**m1**−**m7**) in two monomer concentration conditions. The control mixture (**m0**) contains AA as the only functional monomer and was used to test the TC-binding capacity of the assayed mixtures. The total interaction energy (E_{total}) was obtained as the sum of electrostatic (E_{elec}) and van der Waals (E_{vdW}) contributions, calculated for the interaction between the template (TC) and the surrounding monomers within a cutoff distance of 12 Å. Data were obtained from the analysis of 300 ns MD trajectories.

engage in stronger dispersive interactions with the template than AA. On the other hand, E_{elec} showed marked variations between mixtures at both monomer concentrations, with mean values ranging from −2 to −15 kcal/mol (low monomer concentration) and −3 to −30 kcal/mol (high monomer concentration). These results reveal the sensitivity of electrostatic interactions to small changes in mixtures composition. At low monomer concentration conditions, only **m4** results in a significant reduction of E_{elec} (−15.2 ± 1.0 kcal/mol) compared with **m0** (−7.5 ± 0.7 kcal/mol). This mixture contains 40% AA and 40% APMA, which are charged monomers that can engage in attractive electrostatic interactions with polar moieties of the template. This mixture also contains minor proportions of NIPAM and TBAM, which contribute to E_{elec} through amide moieties capable of hydrogen bonding. This suggests that E_{elec} drives the binding to the template in **m4** at low monomer concentration conditions, with a major contribution of charged monomers in interplay with neutral polar monomers. At high monomer concentration conditions, **m1** (−22.4 ± 1.3 kcal/mol) and **m3** (−29.4 ± 1.4 kcal/mol) have more favorable E_{elec} terms than the control **m0** (−11.9 ± 0.9 kcal/mol), whereas other mixtures show weakened electrostatic interactions arising from the screening of

electrostatic interactions by concentration. In these conditions, the mixtures **m1** and **m3** with higher proportions of neutral monomers NIPAM (40%) and TBAM (40%), and minor ratios of charged monomers (AA or APMA) show the best interaction performance with the template. Overall, the total interaction energy (E_{total}) terms show similar trends to E_{elec} at both monomer concentration conditions and suggest the potential of **m1**, **m3**, and **m4** as suitable formulations to achieve more favorable intermolecular interactions with the template and, thereby, more stable pre-polymerization complexes. However, only **m3** and **m4** have AA in their composition, which is critical for our experimental design to enable the covalent conjugation of the photosensitizer on the nanomaterial surface. Thereby, **m1** was discarded for further consideration.

Structural analysis of the pre-polymerization complexes formed in the most promissory mixtures revealed that electrostatic interactions in **m4** (low monomer concentration) are mostly driven by the cationic monomer APMA, which interacts with carbonyl moieties of the template through its 3-aminopropyl side chain at heteroatomic distances ∼2−3 Å, consistent with hydrogen bond formation (Figure 4). On the other hand, AA interacts with the cationic *N,N*-dimethylamino
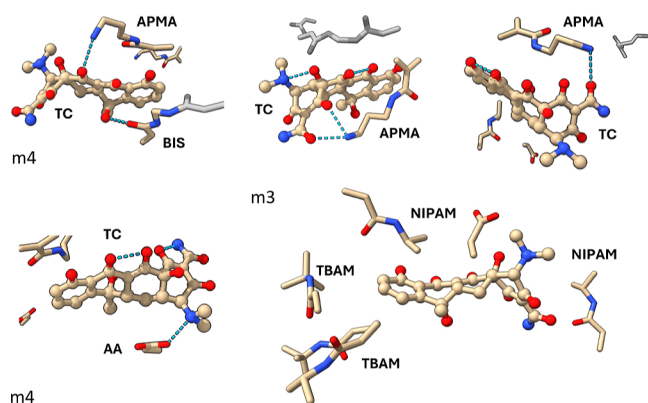
Figure 4. Close-up of pre-polymerization complexes sampled from 300 ns MD simulations in mixtures **m4** (low monomer concentration) and **m3** (high monomer concentration). For **m4**, the structures show the electrostatic contacts mediated by APMA and AA with polar moieties of the template. For **m3**, the selected snapshot shows the involvement of NIPAM and TBAM in hydrophobic contacts with the template. The template TC is displayed in ball-and-stick representations, whereas the functional monomers APMA, AA, NIPAM, and TBAM are shown as line representations. For better visualization, water molecules and other interacting monomers in each snapshot were not shown.

group of TC throughout the simulated MD trajectory. In the case of **m3** (high monomer concentration), the increased NIPAM and TBAM ratios translate into stronger van der Waals interactions between their hydrophobic side chains and the TC as major driving forces for the pre-polymerization complexes in this mixture.

Additional information regarding the imprinting capacity of the tested formulations was obtained by measuring the extent to which the monomer mixture organizes around the template to form pre-polymerization complexes in each MD trajectory. To this end, we calculated the monomer shell as the sum of monomer or cross-linker units interacting with the template at distances < 10 Å in each simulation frame. Figure 5 reports monomer shell distributions for the mixtures **m0**−**m7** at two monomer concentration conditions. Our findings revealed that **m1**−**m7** have denser monomer shells (i.e., mean values shifted to a higher number of monomers surrounding the template) than **m0**, which suggests better imprinting capacities than the control formulation. Nevertheless, no significant differences in

the monomer shell distributions among **m1**−**m7** were observed at both monomer concentration conditions despite their differential energetic profiles regarding template−monomer interaction energies (Figure 3). This analysis supports the decisive role of the energetics of pre-polymerization complex formation in differentiating the molecular imprinting potential of monomer mixtures with different compositions. Based on these considerations, we chose the mixtures **m4** and **m3** to continue with the synthesis and experimental evaluation of photoactive MINs synthesis with the dual capacity of binding TC and promoting its degradation under visible light irradiation, as detailed in the following section.

3.2. Synthesis and Characterization of Photoactive MINs.

MINs were synthesized via high-dilution radical polymerization in an aqueous medium using monomer feed ratios corresponding to mixtures **m3** and **m4** (Table 2). Parallel polymerization reactions were carried out in template-free mixtures to obtain nINs of identical composition to MINs. The crude polymers were surface conjugated with an organic photosensitizer to achieve photoactive materials. To that aim, we chose toluidine blue (TOL), which is a cheap, highly soluble, nontoxic, and well-characterized cationic thiazine dye that generates high yields of singlet oxygen ($^1O_2$) in aqueous solution under visible light irradiation (λ_{max} = 628−633 nm) with a type-II photosensitization mechanism.[56] TOL has been extensively used in photodynamic applications either in solution or as part of conjugated nanomaterials, and thereby it is a proven choice to confer photodynamic properties to our molecularly imprinted and non-imprinted materials.[57−60] TOL conjugation was achieved through its aromatic amino moiety via EDC/NHS coupling with the carboxyl side chain of AA within the polymers (Figure 6A). The conjugated materials were thoroughly purified by dialysis to remove the template, unreacted monomers, low molecular weight oligomers, the fraction of non-conjugated TOL, and other reaction by-products. Our final products were aqueous dispersions of two MINs (**MIN3** and **MIN4**) and their non-imprinted counterparts (**nIN3** and **nIN4**) at concentrations ranging from 0.44−1.18 mg mL^{-1} with estimated TOL loadings of ~10% in weight.

The polymer dispersions were characterized by DLS experiments, which confirmed the nanoscale dimensions of both molecularly imprinted and non-imprinted materials.
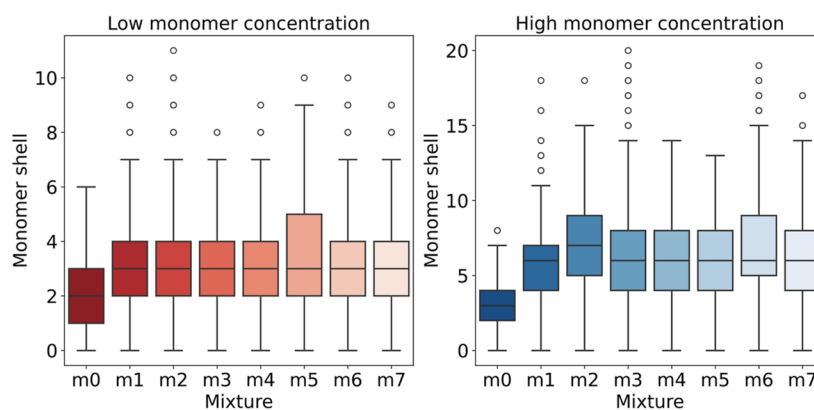

Figure 5. Monomer shell distributions calculated for pre-polymerization mixtures **m0**−**m7** in two monomer concentration conditions. Monomer shells were calculated as the sum of monomer (NIPAM, TBAM, AA, APMA) or cross-linker (BIS) units interacting with the template (TC) at distances <10 Å throughout 600 frames retrieved from 300 ns MD simulations.
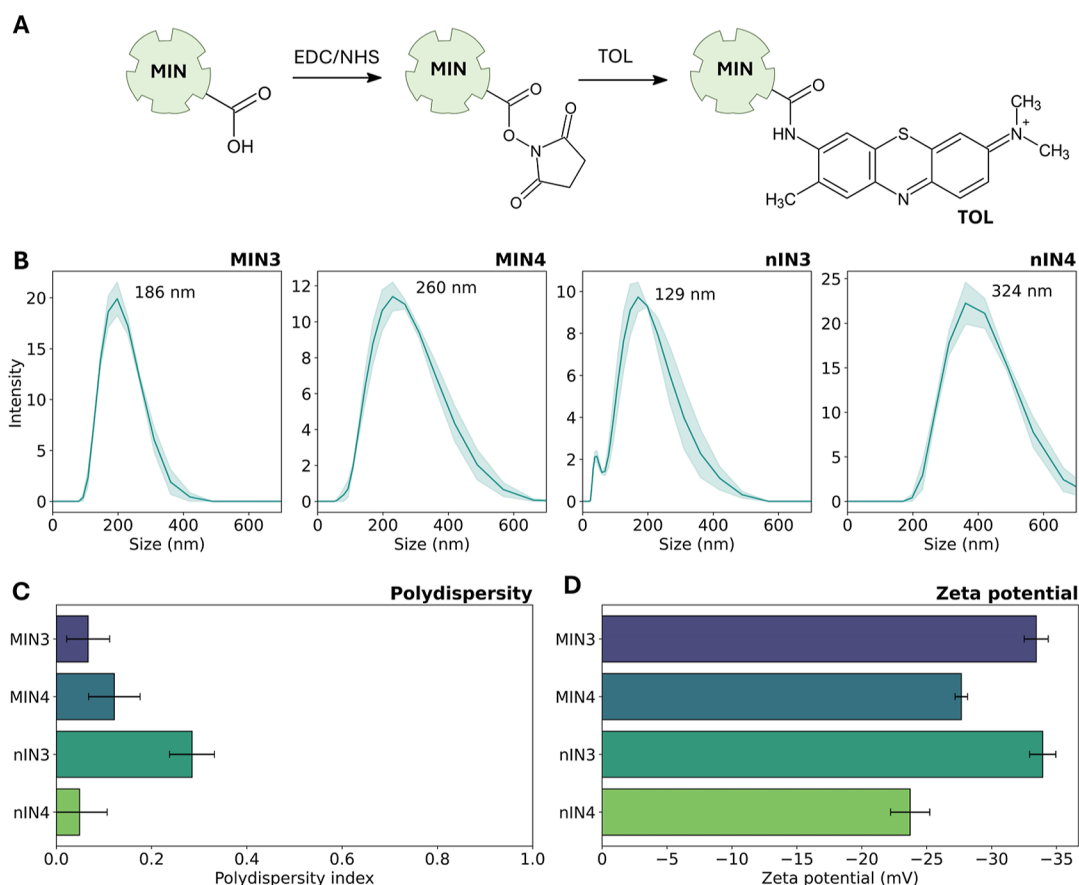
Figure 6. (A) Schematic illustration for the surface conjugation of MINs with toluidine blue (TOL) via EDC/NHS coupling to achieve photoactive MINs. An identical procedure was applied to obtain TOL-conjugated nINs with identical composition to MINs. (B) Nanoparticle size distribution obtained from DLS experiments for aqueous dispersions of photoactive MINs (**MIN3** and **MIN4**) and non-imprinted counterparts (**nIN3** and **nIN4**). Data is reported as the average of three independent measurements. (C) Polydispersity indexes obtained from DLS experiments for photoactive MINs (**MIN3** and **MIN4**) and non-imprinted counterparts (**nIN3** and **nIN4**). (D) Average zeta potential (mV) for photoactive MINs (**MIN3** and **MIN4**) and non-imprinted counterparts (**nIN3** and **nIN4**). Mean values obtained from three independent measurements and their corresponding standard deviations are reported.

Mean nanoparticle diameters ranged from 180 to 260 nm for MINs and 129−324 nm for nINS (Figure 6B). These dimensions ensure high surface areas per mass unit, required for rebinding the template in subsequent experiments.[61] Polydispersity indexes (PI) indicate narrow molecular weight distributions, with PI values ranging between 0.05 and 0.29 for MINs and nINs (Figure 6C). These values are consistent with the expected outcomes of high-dilution polymerization in nanopolymer synthesis.[62] The prepared nanomaterials have negative zeta potentials ranging from −24 to −34 mV. These magnitudes account for moderate-to-high dispersion stabilities with low aggregation propensity due to strong electrostatic repulsions between equally charged nanoparticles.[63,64] Electrostatic repulsion will counter the natural tendency of polymeric nanoparticles to aggregate due to van der Waals interactions, which will translate into dispersion stability over time. These findings are encouraging to continue with the next step in our rational design strategy, in which the nanoparticles will be tested for their ability to rebind the template and generate reactive oxygen species under visible light irradiation, as detailed in the following sections.

3.3. TC Rebinding Tests. Aqueous dispersions of the polymeric nanoparticles **MIN3**, **MIN4**, **nIN3**, and **nIN4** at identical volumes and concentrations (200 μL, 0.1 mg mL^{-1}) were placed into polystyrene microplate wells and carefully

dried to immobilize the nanomaterials by physical adsorption on the microplate surface. The immobilized nanoparticles were washed with ethanol to remove any residual template or unconjugated photosensitizer that may have remained after the dialysis purification process. The nanomaterials were then contacted with TC 50 μmol L^{-1} solutions to evaluate their capacity to rebind the template. The percentage of TC rebinding was calculated by measuring the residual TC content in the supernatant solution after 12 h of contact. In this regard, it is worth reminding that TC can bind to either MINs or nINs, as both polymeric materials share identical monomeric components with chemically diverse functional groups capable of engaging in nonspecific electrostatic, hydrogen bonding, van der Waals and π-interactions with the template. Nevertheless, the molecularly imprinted cavities on the MINs surface are expected to enhance the TC rebinding capacity of these materials over non-imprinted counterparts. Our findings confirmed this prediction, showing that **MIN3** (38%) and **MIN4** (45%) have higher TC rebinding percentages than their corresponding non-imprinted materials **nIN3** (16%) and **nIN4** (12%) (Figure 7). A large variability between independent experiments was observed for **MIN3** and **nIN4**, which was attributed to the heterogeneous distribution of immobilized nanoparticles on the microplate well surfaces and the potential washout loss of weakly immobilized nanopolymers. These
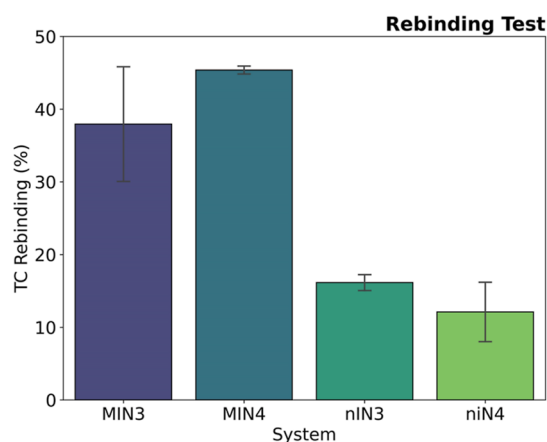
Figure 7. Template rebinding assays for immobilized MINs and nINS. Nanoparticles were immobilized onto polystyrene microplate wells and contacted with TC 50 μmol L^{-1} solutions for 12 h. The percentage of TC rebinding was calculated by measuring the remaining TC content in the supernatant solution. Experiments were carried out in triplicate. Percentages are reported as mean values with their corresponding standard deviations.

limitations will be addressed in our future studies to maximize the adsorption efficiency and homogeneity of the immobilization process.

3.4. Singlet Oxygen Generation Experiments.
Singlet oxygen generation experiments were carried out to test the photodynamic activity of the polymeric nanomaterials (**MIN3**, **MIN4**, **nIN3**, and **nIN4**) under visible light irradiation. Singlet oxygen is the primary reactive oxygen species (ROS) that is expected from type-II photosensitizers like TOL. Therefore, we focused our interest in this species to account for the capacity of the nanomaterials to trigger oxidative processes after being irradiated. Experiments were conducted in black-bottom microplate wells where the nanoparticles **MIN3**, **MIN4**, **nIN3**, and **nIN4** were physically immobilized. Before conducting the assays, the wells were carefully washed with ethanol to remove any remnant of non-conjugated TOL. The immobilized nanomaterials were contacted with an aqueous solution of the commercial singlet oxygen detection sensor (SOSG) and irradiated with a visible light LED lamp (150 W

m^{-2}) for 60 min. The emission spectrum of the LED light source shows a maximum irradiance peak at around 600 nm, which ensures the photoexcitation of the photosensitizer (Figure S1). The singlet oxygen production in each well was followed by fluorescence intensity measurements (excitation wavelength of 485 nm and emission wavelength of 520 nm) at increasing irradiation times (Figure 8A). Our findings revealed that MINs and nINS have similar singlet oxygen generation capacities arising from equivalent TOL conjugation ratios. Therefore, molecularly imprinted and non-imprinted nanomaterials can trigger oxidative processes under visible light irradiation. Parallel experiments with the commercial HPF sensor for hydroxyl radical detection revealed a minor production of this species under identical irradiation conditions, confirming the predominant role of singlet oxygen as the major photodynamic product for MINs and nINs (Figure 8B).

3.5. TC Degradation Mediated by Photoactive MINs.
Photoactive polymeric nanomaterials were tested for their ability to promote TC degradation under visible light irradiation. In this regard, the imprinted cavities in **MIN3** and **MIN4** are expected to enhance degradation by bringing the template close to the photosensitizer moieties, maximizing the oxidative potential of the generated ROS. TC degradation experiments were carried out in polystyrene microplates containing immobilized nanoparticles (**MIN3**, **MIN4**, **nIN3**, and **nIN4**). The wells were carefully washed with ethanol to remove any impurities, as was done in the previous experiments, and contacted with TC 50 μmol L^{-1} solutions. The systems were irradiated with a visible light LED lamp (150 W m^{-2}) for 60 min, and the remaining TC concentration in solution was followed by UV−vis spectra measurements at 15 min intervals (Figure S2). Control experiments were conducted in nanoparticle-free wells to measure the extent of TC photodegradation without photoactive materials. Degradation profiles were built from absorbance variation at λ_{max} (360 nm) as a function of the irradiation time (Figure 9A). Our findings revealed that TC degraded faster and to a larger extent in wells containing molecularly imprinted materials **MIN3** (29%) and **MIN4** (57%) than in systems treated with analogous non-imprinted counterparts **nIN3** (23%) and **nIN4** (25%), whereas minimum degradation was detected in control
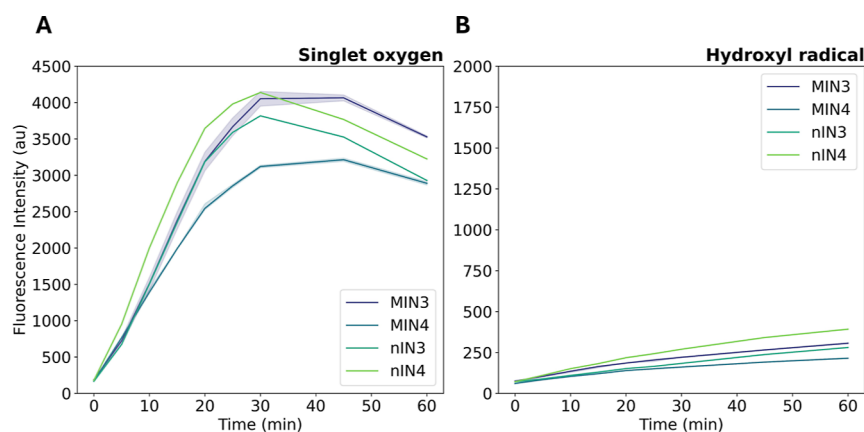

Figure 8. Singlet oxygen (A) and hydroxyl radical (B) generation experiments for molecularly imprinted (**MIN3** and **MIN3**) and non-molecularly imprinted (**nIN3**, **nIN4**) nanoparticles. Experiments were conducted in microplate wells containing immobilized nanoparticles, irradiated with visible LED light for 60 min. The release of singlet oxygen and hydroxyl radical was followed by fluorescence intensity measurements using the commercial sensors SOSG and HPF, respectively. Experiments were carried out in triplicate.
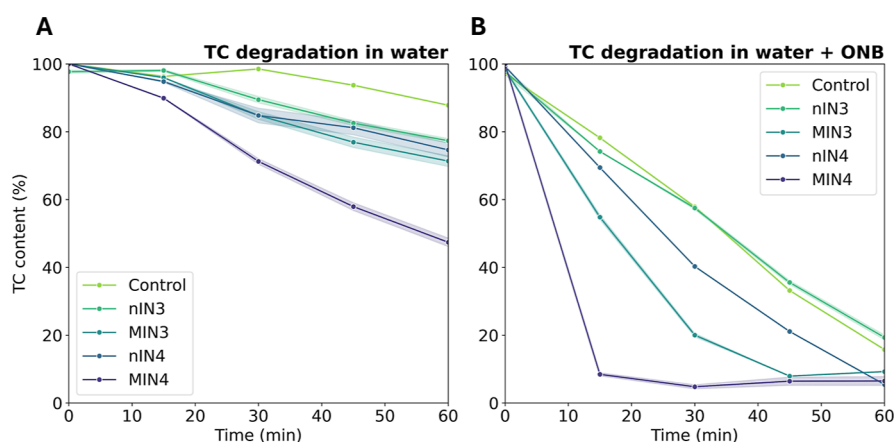
Figure 9. (A) TC degradation profiles measured from the absorbance (λ_{max} = 360 nm) variation of TC 50 μmol L^{-1} solutions in contact with molecularly imprinted (**MIN3** and **MIN4**) and non-molecularly imprinted (**nIN3** and **nIN4**) nanoparticles as a function of the irradiation time. Control experiments were conducted with TC 50 μmol L^{-1} in nanoparticle-free wells under identical irradiation conditions. All experiments were carried out in triplicate. (B) TC degradation profiles for TC 50 μmol L^{-1} solutions supplemented with oxygen nanobubbles (ONB). Solutions were contacted with immobilized polymeric nanoparticles (**MIN3**, **MIN4**, **nIN3**, and **nIN4**) and irradiated with a visible light LED lamp (150 W m^{-2}) for 60 min. Control experiments were carried out in nanoparticle-free wells under identical irradiation conditions. All experiments were performed in triplicate.

systems (<10%). Degradation profiles followed pseudozero-order kinetics, which suggests that reaction rates are limited by the binding of TC at active sites on the nanomaterial surface, where maximum ROS concentrations are expected (Table 3).

Table 3. Pseudo-Zero-Order Kinetic Constants k_{cin} (nM s^{-1}) for TC Degradation Under Visible Light Irradiation Assisted by Molecularly Imprinted (MIN3 and MIN4) and Non-Imprinted (nIN3 and nIN4) Nanoparticles[a]

system	k_{cin} (nM s^{-1})	maximum TC degradation (%)	t_{max} (min)
control		<10%	60
nIN3	6.3	23 ± 5	60
nIN4	7.1	25 ± 11	60
MIN3	8.4	29 ± 11	60
MIN4	16.5	57 ± 11	60
ONB (control)	23.0	84 ± 4	60
nIN3 + ONB	21.7	81 ± 5	60
nIN4 + ONB	26.2	94 ± 3	60
MIN3 + ONB	33.9	>95%	45
MIN4 + ONB	101	>95%	15

[a]Maximum TC degradation (%) is the highest percentage of TC degradation achieved at $t_{max} \leq$ 60 min, starting with TC 50 μmol L^{-1} solutions. ONB stands for experiments conducted in TC solutions supplemented with oxygen nanobubbles.

Thereby, the enhanced degradation efficiency by **MIN3** and **MIN4** can be attributed to the specific binding of TC at molecularly imprinted cavities, minimizing the loss of oxidative potential due to ROS diffusion or deactivation.[65,66] **MIN4** showed a better performance in promoting TC than **MIN3**, in line with the TC rebinding capacity of these nanomaterials (Figure 7). Regarding degradation products, literature reports have shown that the oxidative processes triggered by singlet oxygen and other ROS result in low molecular weight nontoxic compounds.[67−69] The proposed degradation pathways involve the oxidation of the *N,N*-dimethyl group into a carbonyl derivative and the subsequent removal of the amide moiety in ring A, followed by subsequent ring fragmentations.[67−69]

To further test the degradation efficacy mediated by photoactive polymeric nanoparticles, we conducted additional photodegradation experiments using TC solutions supplemented with oxygen nanobubbles (ONBs). ONBs are stable nanoscale aggregates of molecular oxygen with intrinsic photodynamic activity and promissory applications as enhancers of advanced oxidation processes without secondary pollution effects at minimal costs.[70−74] ONBs have been reported to improve the photodegradation of antibiotic pollutants such as oxytetracycline under visible light through "high mass transfer and generation of reactive radicals during the nanobubble collapse" including hydroxyl radical, superoxide radical, and singlet oxygen.[75] ONBs have also been reported to interact strongly with positive nanoparticles by nucleation at the solid−liquid interface.[76,77] This evidence offers the opportunity to test whether ONBs can synergize with MINs to achieve higher TC degradation ratios. To this end, we prepared fresh TC 50 mmol L^{-1} solutions using ONB-supplemented water and placed them in microplate wells containing immobilized nanoparticles (**MIN3**, **MIN4**, **nIN3**, and **nIN4**). Control experiments were conducted in nanoparticle-free wells with ONB-supplemented TC solutions. Systems were irradiated under identical conditions to previous photodegradation experiments for 60 min. TC degradation profiles confirmed the intrinsic oxidative potential of ONBs, which achieved a maximum degradation of 84% at 60 min of irradiation (Figure 9B). Solutions contacted with **nIN3** (81%) showed almost identical degradation profiles to the control, while **nIN4** (94%) exhibited a slightly higher degradation efficacy. On the other hand, **MIN3** (>95%) and **MIN4** (>95%) showed almost complete degradation ratios at irradiation times significantly shorter than the control. In solutions contacted with **MIN3**, the maximum TC degradation was achieved at 45 min of irradiation, whereas in systems contacted with **MIN4**, TC degradation took only 15 min to take place completely. These findings confirm the synergism between MINs and ONBs and represent a significant advancement compared to recent studies on the photocatalytic degradation of TC under visible light. For instance, the use of Cu$_2$O−TiO$_2$ nanotubes has achieved the complete removal of TC in water after 60 min

of irradiation.[67] Other reports using titania, black anatase, or titania dopped with acetylene black, and persulfate have shown degradation efficacies close to ~60% with irradiation times ranging from 60 to 240 min[68,78,79]

4. CONCLUSIONS

Molecular dynamics simulations guided the selection of monomer formulations to develop molecularly imprinted nanoparticles for TC binding. Template-monomer interaction energies resulted in significant variations within different monomer formulations, which supports the sensitivity of force field-based intermolecular interaction calculations to small changes in mixture composition. Template-monomer interaction energies also responded to concentration changes, accounting for the screening of electrostatic contacts at high monomer concentration conditions. The formulations with the highest theoretical potential resulted in molecularly imprinted nanomaterials with higher TC binding capacities than non-imprinted counterparts of identical composition. This supports the relevance of the template-shaped cavities in enhancing the interaction with TC over nonspecific interactions with the polymer components. Molecularly imprinted and non-imprinted nanoparticles have photodynamic activity under visible light irradiation, provided by surface conjugation with an organic photosensitizer. The dual capacity of molecularly imprinted nanopolymers to bind TC and release reactive oxygen species under visible light irradiation potentiates the degradation of the template by minimizing the loss of oxidative power due to diffusion. These materials synergize with oxygen nanobubbles in promoting TC degradation by visible light, which highlights the potential of MIP-based photodegradation strategies to address any other pollutant for which molecular imprinting is achievable.

■ ASSOCIATED CONTENT

Ⓢ Supporting Information

The Supporting Information is available free of charge at https://pubs.acs.org/doi/10.1021/acsomega.4c04550.

> All simulation and analysis scripts for molecular dynamics simulations, the emission spectrum of the visible light LED lamp used in this study, UV–vis spectra for TC solutions in TC degradation experiments (PDF)

■ AUTHOR INFORMATION

Corresponding Author

    Verónica A. Jiménez − *Departamento de Ciencias Químicas, Facultad de Ciencias Exactas, Universidad Andres Bello, Talcahuano 7100, Chile;* ⓞ orcid.org/0000-0002-6783-5657; Email: veronica.jimenez@unab.cl

Authors

    Yadiris García − *Departamento de Ciencias Químicas, Facultad de Ciencias Exactas, Universidad Andres Bello, Talcahuano 7100, Chile*

    Joao Aguilar − *Departamento de Ciencias Químicas, Facultad de Ciencias Exactas, Universidad Andres Bello, Talcahuano 7100, Chile*

    Laura Polania − *Departamento de Ciencias Químicas, Facultad de Ciencias Exactas, Universidad Andres Bello, Talcahuano 7100, Chile;* ⓞ orcid.org/0000-0001-9873-7999

    Yorley Duarte − *Center for Bioinformatics and Integrative Biology (CBIB), Facultad de Ciencias de la Vida, Universidad Andres Bello, Santiago 8370146, Chile*

    Börje Sellergren − *Surecapture Technologies AB, Malmö 214 32, Sweden; Biofilms Research Center for Biointerfaces, Malmö University, Malmö 214 32, Sweden;* ⓞ orcid.org/0000-0002-2392-3305

Complete contact information is available at:
https://pubs.acs.org/10.1021/acsomega.4c04550

Author Contributions

The manuscript was written through contributions of all authors. All authors have given approval to the final version of the manuscript.

Notes

The authors declare no competing financial interest.

■ ACKNOWLEDGMENTS

■ ABBREVIATIONS

MIN, molecularly imprinted nanoparticles; nIN, non-imprinted nanoparticles; ROS, reactive oxygen species; TC, tetracycline

■ REFERENCES

(1) Gothwal, R.; Shashidhar, T. Antibiotic Pollution in the Environment: A Review. *Clean: Soil, Air, Water* **2015**, *43* (4), 479−489.

(2) Danner, M.-C.; Robertson, A.; Behrends, V.; Reiss, J. Antibiotic Pollution in Surface Fresh Waters: Occurrence and Effects. *Sci. Total Environ.* **2019**, *664*, 793−804.

(3) Dai, Y.; Liu, M.; Li, J.; Yang, S.; Sun, Y.; Sun, Q.; Wang, W.; Lu, L.; Zhang, K.; Xu, J.; et al. A Review on Pollution Situation and Treatment Methods of Tetracycline in Groundwater. *Sep. Sci. Technol.* **2020**, *55* (5), 1005−1021.

(4) Amangelsin, Y.; Semenova, Y.; Dadar, M.; Aljofan, M.; Bjørklund, G. The Impact of Tetracycline Pollution on the Aquatic Environment and Removal Strategies. *Antibiotics* **2023**, *12* (3), 440.

(5) Chen, Y.; Hu, C.; Qu, J.; Yang, M. Photodegradation of Tetracycline and Formation of Reactive Oxygen Species in Aqueous Tetracycline Solution Under Simulated Sunlight Irradiation. *J. Photoch. Photobio. A* **2008**, *197* (1), 81−87.

(6) Wang, H.; Li, J.; Zhou, M.; Guan, Q.; Lu, Z.; Huo, P.; Yan, Y. Preparation and Characterization of Ag2O/SWNTs Photocatalysts and its Photodegradation on Tetracycline. *J. Ind. Eng. Chem.* **2015**, *30*, 64−70.

(7) López-Peñalver, J. J.; Sánchez-Polo, M.; Gómez-Pacheco, C. V.; Rivera-Utrilla, J. Photodegradation of Tetracyclines in Aqueous Solution by Using UV and UV/H2O2 Oxidation Processes. *J. Chem. Technol. Biot.* **2010**, *85* (10), 1325−1333.

(8) Ao, W.; Qu, J.; Yu, H.; Liu, Y.; Liu, C.; Fu, J.; Dai, J.; Bi, X.; Yuan, Y.; Jin, Y. TiO2/Activated Carbon Synthesized by Microwave-assisted Heating for Tetracycline Photodegradation. *Environ. Res.* **2022**, *214*, 113837.

(9) Gómez-Pacheco, C. V.; Sánchez-Polo, M.; Rivera-Utrilla, J.; López-Peñalver, J. J. Tetracycline Degradation in Aqueous Phase by Ultraviolet Radiation. *Chem. Eng. J.* **2012**, *187*, 89−95.

(10) Cai, T.; Ma, M.; Liu, H.; Li, J.; Hou, J.; Gong, B. Preparation of Monodisperse Magnetic Surface Molecularly Imprinted Polymers for Selective Recognition of Lincomycin Hydrochloride in Milk. *J. Liq. Chromatogr. Relat. Technol.* **2019**, *42* (13−14), 459−467.

(11) Negarian, M.; Mohammadinejad, A.; Mohajeri, S. A. Preparation, Evaluation and Application of Core-Shell Molecularly Imprinted Particles as the Sorbent in Solid-Phase Extraction and Analysis of Lincomycin Residue in Pasteurized Milk. *Food Chem.* **2019**, *288*, 29−38.

(12) Li, Z.; Lei, C.; Wang, N.; Jiang, X.; Zeng, Y.; Fu, Z.; Zou, L.; He, L.; Liu, S.; Ao, X.; et al. Preparation of Magnetic Molecularly Imprinted Polymers with Double Functional Monomers for the Extraction and Detection of Chloramphenicol in Food. *J. Chromatogr. B Biomed. Sci. Appl.* **2018**, *1100−1101*, 113−121.

(13) Lian, Z.; Wang, J. Selective Detection of Chloramphenicol Based on Molecularly Imprinted Solid-Phase Extraction in Seawater from Jiaozhou Bay, China. *Mar. Pollut. Bull.* **2018**, *133*, 750−755.

(14) Huang, L.; Yu, W.; Guo, X.; Huang, Y.; Zhou, Q.; Zhai, H. Chip-based Multi-Molecularly Imprinted Monolithic Capillary Array Columns Coated Fe3O4/GO for Selective Extraction and Simultaneous Determination of Tetracycline, Chlortetracycline and Deoxytetracycline in Eggs. *Microchem. J.* **2019**, *150*, 104097.

(15) Guo, M.; Wang, R.; Jin, Z.; Zhang, X.; Jokerst, J. V.; Sun, Y.; Sun, L. Hyperbranched Molecularly Imprinted Photoactive Polymers and Its Detection of Tetracycline Antibiotics. *ACS Appl. Polym. Mater.* **2022**, *4* (2), 1234−1242.

(16) Ma, N.; Feng, C.; Qu, P.; Wang, G.; Liu, J.; Liu, J. X.; Wang, J. P. Determination of Tetracyclines in Chicken by Dispersive Solid Phase Microextraction Based on Metal-Organic Frameworks/ Molecularly Imprinted Nano-polymer and Ultra Performance Liquid Chromatography. *Food Anal. Methods* **2020**, *13* (5), 1211−1219.

(17) Song, X.; Zhou, T.; Li, J.; Su, Y.; Xie, J.; He, L. Determination of Macrolide Antibiotics Residues in Pork Using Molecularly Imprinted Dispersive Solid-Phase Extraction Coupled with LC-MS/ MS. *J. Sep. Sci.* **2018**, *41* (5), 1138−1148.

(18) Pupin, R. R.; Foguel, M. V.; Gonçalves, L. M.; Sotomayor, M. d. P. T. Magnetic molecularly imprinted polymers obtained by photopolymerization for selective recognition of penicillin G. *J. Appl. Polym. Sci.* **2020**, *137* (13), 48496.

(19) Tian, Y.; Wang, Y.; Wu, S.; Sun, Z.; Gong, B. Preparation of Ampicillin Surface Molecularly Imprinted Polymers for Its Selective Recognition of Ampicillin in Eggs Samples. *Int. J. Anal. Chem.* **2018**, *2018*, 5897381.

(20) Zhu, G.; Cheng, G.; Wang, P.; Li, W.; Wang, Y.; Fan, J. Water Compatible Imprinted Polymer Prepared in Water for Selective Solid Phase Extraction and Determination of Ciprofloxacin in real samples. *Talanta* **2019**, *200*, 307−315.

(21) Urraca, J. L.; Hall, A. J.; Moreno-Bondi, M. C.; Sellergren, B. A Stoichiometric Molecularly Imprinted Polymer for the Class-Selective Recognition of Antibiotics in Aqueous Media. *Angew. Chem., Int. Ed. Engl.* **2006**, *45* (31), 5158−5161.

(22) Urraca, J. L.; Moreno-Bondi, M. C.; Hall, A. J.; Sellergren, B. Direct extraction of Penicillin G and Derivatives from Aqueous Samples Using a Stoichiometrically Imprinted Polymer. *Anal. Chem.* **2007**, *79* (2), 695−701.

(23) Benito-Peña, E.; Urraca, J. L.; Sellergren, B.; Moreno-Bondi, M. C. Solid-phase Extraction of Fluoroquinolones from Aqueous Samples Using a Water-Compatible Stochiometrically Imprinted Polymer. *J. Chromatogr. A* **2008**, *1208* (1−2), 62−70.

(24) Cai, W.; Gupta, R. B. Molecularly-Imprinted Polymers Selective for Tetracycline Binding. *Sep. Purif. Technol.* **2004**, *35* (3), 215−221.

(25) Suedee, R.; Srichana, T.; Chuchome, T.; Kongmark, U. Use of Molecularly Imprinted Polymers from a Mixture of Tetracycline and its Degradation Products to Produce Affinity Membranes for the Removal of Tetracycline from Water. *J. Chromatogr. B Biomed. Sci. Appl.* **2004**, *811* (2), 191−200.

(26) Pupin, R. R.; Sotomayor, M. D. P. T. Synthesis and Evaluation of Hollow Porous Molecularly Imprinted Polymer for Selective Determination of Tetracycline. *J. Mater. Sci.* **2022**, *57* (36), 17291−17303.

(27) Caro, E.; Marcé, R. M.; Cormack, P. A. G.; Sherrington, D. C.; Borrull, F. Synthesis and Application of an Oxytetracycline Imprinted Polymer for the Solid-Phase Extraction of Tetracycline Antibiotics. *Anal. Chim. Acta* **2005**, *552* (1−2), 81−86.

(28) Sánchez-Polo, M.; Velo-Gala, I.; López-Peñalver, J. J.; Rivera-Utrilla, J. Molecular Imprinted Polymer to Remove Tetracycline from Aqueous Solutions. *Micropor. Mesopor. Mater.* **2015**, *203*, 32−40.

(29) Wang, L.-Q.; Lin, F.-Y.; Yu, L.-P. A Molecularly Imprinted Photonic Polymer Sensor with High Selectivity for Tetracyclines Analysis in Food. *Analyst* **2012**, *137* (15), 3502−3509.

(30) Feng, M. X.; Wang, G. N.; Yang, K.; Liu, H. Z.; Wang, J. P. Molecularly Imprinted Polymer-High Performance Liquid Chromatography for the Determination of Tetracycline Drugs in Animal Derived Foods. *Food Control* **2016**, *69*, 171−176.

(31) Ma, Y.; Liao, X.; Zhao, Y.; Qiu, L.; Yao, Y.; Wang, S.; Yang, X.; Hu, X. Fabrication of magnetic molecularly imprinted polymers based on aptamers and β-cyclodextrin for synergistic recognition and separation of tetracycline. *Anal. Chim. Acta* **2022**, *1236*, 340572.

(32) Rajpal, S.; Mishra, P.; Mizaikoff, B. Rational In Silico Design of Molecularly Imprinted Polymers: Current Challenges and Future Potential. *Int. J. Mol. Sci.* **2023**, *24* (7), 6785.

(33) Olsson, G. D.; Wiklander, J. G.; Nicholls, I. A. Using Molecular dynamics (MD) in the Study of Molecularly Imprinted Polymers (MIP). In *Molecularly Imprinted Polymers: Methods and Protocols*; Martín-Esteban, A., Ed.; Springer US, 2021; pp 241−268.

(34) Subrahmanyam, S.; Piletsky, S. A.; Piletska, E. V.; Chen, B.; Karim, K.; Turner, A. P. F. 'Bite-and-Switch' approach using computationally designed molecularly imprinted polymers for sensing of creatinine11Editors Selection. *Biosen. Bioelectron.* **2001**, *16* (9−12), 631−637.

(35) Chianella, I.; Lotierzo, M.; Piletsky, S. A.; Tothill, I. E.; Chen, B.; Karim, K.; Turner, A. P. F. Rational Design of a Polymer Specific for Microcystin-LR Using a Computational Approach. *Anal. Chem.* **2002**, *74* (6), 1288−1293.

(36) Baggiani, C.; Anfossi, L.; Baravalle, P.; Giovannoli, C.; Tozzi, C. Selectivity Features of Molecularly Imprinted Polymers Recognising the Carbamate Group. *Anal. Chim. Acta* **2005**, *531* (2), 199−207.

(37) Bates, F.; Busato, M.; Piletska, E.; Whitcombe, M. J.; Karim, K.; Guerreiro, A.; del Valle, M.; Giorgetti, A.; Piletsky, S. Computational Design of Molecularly Imprinted Polymer for Direct Detection of Melamine in Milk. *Sep. Sci. Technol.* **2017**, *52* (8), 1441−1453.

(38) Viveiros, R.; Karim, K.; Piletsky, S. A.; Heggie, W.; Casimiro, T. Development of a Molecularly Imprinted Polymer for a Pharmaceutical Impurity in Supercritical CO2: Rational Design Using Computational Approach. *J. Clean. Prod.* **2017**, *168*, 1025−1031.

(39) Zink, S.; Moura, F. A.; Autreto, P. A. d. S.; Galvão, D. S.; Mizaikoff, B. Virtually Imprinted Polymers (VIPs): Understanding Molecularly Templated Materials via Molecular Dynamics Simulations. *Phys. Chem. Chem. Phys.* **2018**, *20* (19), 13145−13152.

(40) Schillinger, E.; Möder, M.; Olsson, G. D.; Nicholls, I. A.; Sellergren, B. An Artificial Estrogen Receptor Through Combinatorial Imprinting. *Chemistry* **2012**, *18* (46), 14773−14783.

(41) Kong, Y.; Wang, N.; Ni, X.; Yu, Q.; Liu, H.; Huang, W.; Xu, W. Molecular Dynamics Simulations of Molecularly Imprinted Polymer Approaches to the Preparation of Selective Materials to Remove Norfloxacin. *J. Appl. Polym. Sci.* **2016**, *132*, 42817.

(42) García, Y.; Úsuga, B. A.; Campos, C. H.; Alderete, J. B.; Jiménez, V. A. NanoMIPs Design for Fucose and Mannose Recognition: A Molecular Dynamics Approach. *J. Chem. Inf. Model.* **2021**, *61* (4), 2048−2061.

(43) Daniels, E.; Mustafa, Y. L.; Herdes, C.; Leese, H. S. Optimization of Cortisol-Selective Molecularly Imprinted Polymers Enabled by Molecular Dynamics Simulations. *ACS Appl. Bio Mater.* **2021**, *4* (9), 7243−7253.

(44) Cubuk, H.; Ozbil, M.; Cakir Hatir, P. Computational Analysis of Functional Monomers Used in Molecular Imprinting for Promising COVID-19 Detection. *Comput. Theor. Chem.* **2021**, *1199*, 113215.

(45) Villano, A.; Barcaro, G.; Monti, S.; Barbani, N.; Rizzo, A.; Rossin, D.; Rastaldo, R.; Giachino, C.; Cristallini, C. Molecularly Imprinted Nanoparticles towards MMP9 for Controlling Cardiac ECM after Myocardial Infarction: A Predictive Experimental-

Computational Chemistry Investigation. *Biomedicines* **2022**, *10* (9), 2070.

(46) Frisch, M. J.; Trucks, G. W.; Schlegel, H. B.; Scuseria, G. E.; Robb, M. A.; Cheeseman, J. R.; Scalmani, G.; Barone, V.; Petersson, G. A.; Nakatsuji, H.; Li, X.; Caricato, M.; Marenich, A. V.; Bloino, J.; Janesko, B. G.; Gomperts, R.; Mennucci, B.; Hratchian, H. P.; Ortiz, J. V.; Izmaylov, A. F.; Sonnenberg, J. L.; Williams-Young, D.; Ding, F.; Lipparini, F.; Egidi, F.; Goings, J.; Peng, B.; Petrone, A.; Henderson, T.; Ranasinghe, D.; Zakrzewski, V. G.; Gao, J.; Rega, N.; Zheng, G.; Liang, W.; Hada, M.; Ehara, M.; Toyota, K.; Fukuda, R.; Hasegawa, J.; Ishida, M.; Nakajima, T.; Honda, Y.; Kitao, O.; Nakai, H.; Vreven, T.; Throssell, K.; Montgomery, J. A.; Peralta, J. E.; Ogliaro, F.; Bearpark, M. J.; Heyd, J. J.; Brothers, E. N.; Kudin, K. N.; Staroverov, V. N.; Keith, T. A.; Kobayashi, R.; Normand, J.; Raghavachari, K.; Rendell, A. P.; Burant, J. C.; Iyengar, S. S.; Tomasi, J.; Cossi, M.; Millam, J. M.; Klene, M.; Adamo, C.; Cammi, R.; Ochterski, J. W.; Martin, R. L.; Morokuma, K.; Farkas, O.; Foresman, J. B.; Fox, D. J. *Gaussian 16*. Revision C.01; Gaussian, Inc: Wallingford, CT, 2016.

(47) Alguel, Y.; Meng, C.; Terán, W.; Krell, T.; Ramos, J. L.; Gallegos, M.-T.; Zhang, X. Crystal Structures of Multidrug Binding Protein TtgR in Complex with Antibiotics and Plant Antimicrobials. *J. Mol. Biol.* **2007**, *369* (3), 829–840.

(48) Wang, J.; Wolf, R. M.; Caldwell, J. W.; Kollman, P. A.; Case, D. A. Development and Testing of a General Amber Force Field. *J. Comput. Chem.* **2004**, *25* (9), 1157–1174.

(49) Wang, J.; Wang, W.; Kollman, P. A.; Case, D. A. Automatic Atom Type and Bond Type Perception in Molecular Mechanical Calculations. *J. Mol. Graph. Model.* **2006**, *25* (2), 247–260.

(50) Case, D. A.; Aktulga, H. M.; Belfon, K.; Ben-Shalom, I. Y.; Brozell, S. R.; Cerutti, D. S.; Cheatham, T. E. I.; Cruzeiro, V. W. D.; Darden, T. A.; Duke, R. E.; Giambasu, G.; Gilson, M. K.; Gohlke, H.; Goetz, A. W.; Harris, R.; Izadi, S.; Izmailov, S. A.; Jin, C.; Kasavajhala, K.; Kaymak, M. C.; King, E.; Kovalenko, A.; Kurtzman, T.; Lee, T. S.; LeGrand, S.; Li, P.; Lin, C.; Liu, J.; Luchko, T.; Luo, R.; Machado, M.; Man, V.; Manathunga, M.; Merz, K. M.; Miao, Y.; Mikhailovskii, O.; Monard, G.; Nguyen, H.; O'Hearn, K. A.; Onufriev, A.; Pan, F.; Pantano, S.; Qi, R.; Rahnamoun, A.; Roe, D. R.; Roitberg, A.; Sagui, C.; Schott-Verdugo, S.; Shen, J.; Simmerling, C. L.; Skrynnikov, N. R.; Smith, J.; Swails, J.; Walker, R. C.; Wang, J.; Wei, H.; Wolf, R. M.; Wu, X.; Xue, Y.; York, D. M.; Zhao, S.; Kollman, P. A. *AMBER 2021*; University of California: San Francisco, 2021.

(51) Tian, C.; Kasavajhala, K.; Belfon, K. A. A.; Raguette, L.; Huang, H.; Migues, A. N.; Bickel, J.; Wang, Y.; Pincay, J.; Wu, Q.; et al. ff19SB: Amino-Acid-Specific Protein Backbone Parameters Trained against Quantum Mechanics Energy Surfaces in Solution. *J. Chem. Theory Comput.* **2020**, *16* (1), 528–552.

(52) Roe, D. R.; Cheatham, T. E. PTRAJ and CPPTRAJ: Software for Processing and Analysis of Molecular Dynamics Trajectory Data. *J. Chem. Theory Comput.* **2013**, *9* (7), 3084–3095.

(53) Humphrey, W.; Dalke, A.; Schulten, K. VMD: Visual Molecular Dynamics. *J. Mol. Graphics* **1996**, *14* (1), 33–38.

(54) O'Mahony, J.; Wei, S.; Molinelli, A.; Mizaikoff, B. Imprinted Polymeric Materials. Insight into the Nature of Prepolymerization Complexes of Quercetin Imprinted Polymers. *Anal. Chem.* **2006**, *78* (17), 6187–6190.

(55) Babaeipour, V.; Jabbari, F. Pre-polymerization Process Simulation, Synthesis and Investigation the Properties of Dipicolinic Acid Molecularly Imprinted Polymers. *Polym. Bull.* **2023**, *81*, 1495–1512.

(56) Harris, F.; Sayed, Z.; Hussain, S.; Phoenix, D. A. An Investigation Into the Potential of Phenothiazinium-Based Photo-Sensitisers to Act as PDT Agents. *Photodiagnosis Photodyn. Ther.* **2004**, *1* (3), 231–239.

(57) Akhtar, F.; Khan, A. U.; Qazi, B.; Kulanthaivel, S.; Mishra, P.; Akhtar, K.; Ali, A. A Nano Phototheranostic Approach of Toluidine Blue Conjugated Gold Silver Core Shells Mediated Photodynamic Therapy to Treat Diabetic Foot Ulcer. *Sci. Rep.* **2021**, *11* (1), 24464.

(58) Guo, H.; Wang, H.; Deng, H.; Zhang, Y.; Yang, X.; Zhang, W. Facile Preparation of Toluidine Blue-Loaded DNA Nanogels for

Anticancer Photodynamic Therapy. *Front. Bioeng. Biotechnol.* **2023**, *11*, 1180448.

(59) Okkeh, M.; De Vita, L.; Bruni, G.; Doveri, L.; Minzioni, P.; Restivo, E.; Patrini, M.; Pallavicini, P.; Visai, L. Photodynamic Toluidine Blue-gold Nanoconjugates as a Novel Therapeutic for Staphylococcal Biofilms. *RSC Adv.* **2023**, *13* (48), 33887–33904.

(60) Sharma, M.; Visai, L.; Bragheri, F.; Cristiani, I.; Gupta, P. K.; Speziale, P. Toluidine Blue-Mediated Photodynamic Effects on Staphylococcal Biofilms. *Antimicrob. Agents Chemother.* **2008**, *52* (1), 299–305.

(61) Sajini, T.; Mathew, B. A Brief Overview of Molecularly Imprinted Polymers: Highlighting Computational Design, Nano and Photo-Responsive Imprinting. *Talanta Open* **2021**, *4*, 100072.

(62) Sanson, N.; Rieger, J. Synthesis of Nanogels/Microgels by Conventional and Controlled Radical Crosslinking Copolymerization. *Polym. Chem.* **2010**, *1* (7), 965–977.

(63) Gumustas, M.; Sengel-Turk, C. T.; Gumustas, A.; Ozkan, S. A.; Uslu, B. Chapter 5 - Effect of Polymer-Based Nanoparticles on the Assay of Antimicrobial Drug Delivery Systems. In *Multifunctional Systems for Combined Delivery, Biosensing and Diagnostics*; Grumezescu, A. M., Ed.; Elsevier, 2017; pp 67–108.

(64) Honary, S.; Zahir, F. Effect of Zeta Potential on the Properties of Nano-Drug Delivery Systems-A Review (Part 2). *Trop. J. Pharm. Res.* **2013**, *12* (2), 265–273.

(65) Rodgers, M. A. J.; Rossbroich, G.; Garcia, N. A.; Braslavsky, S. E.; Gorman, A. A.; Hamblett, I.; Standen, M. C.; Monici, M. Activated Oxygen. In *Primary Photo-Processes in Biology and Medicine*; Bensasson, R. V., Jori, G., Land, E. J., Truscott, T. G., Eds.; Springer US, 1985; pp 181–207.

(66) Redmond, R. W.; Kochevar, I. E. Symposium-in-Print: Singlet Oxygen Invited Review. *Photochem. Photobiol.* **2006**, *82* (5), 1178–1186.

(67) Sharma, M.; Mandal, M. K.; Pandey, S.; Kumar, R.; Dubey, K. K. Visible-Light-Driven Photocatalytic Degradation of Tetracycline Using Heterostructured $Cu(2)O$-$TiO(2)$ Nanotubes, Kinetics, and Toxicity Evaluation of Degraded Products on Cell Lines. *ACS Omega* **2022**, *7* (37), 33572–33586.

(68) Zhang, T.; Liu, Y.; Rao, Y.; Li, X.; Yuan, D.; Tang, S.; Zhao, Q. Enhanced Photocatalytic Activity of TiO_2 with Acetylene Black and Persulfate for Degradation of Tetracycline Hydrochloride under Visible Light. *Chem. Eng. J.* **2020**, *384*, 123350.

(69) Huang, J.; Li, C.; Hao, H.; Li, L.; Zhu, B.; Chen, X.; Tao, H. Photocatalytic Degradation of Tetracycline Antibiotic over a Flower-Like S-Doped BiOBr: Performance, Mechanism Insight and Toxicity Assessment. *Front. Nanotechnol.* **2022**, *4*, 1023489.

(70) Li, T.; Cui, Z.; Sun, J.; Li, Q.; Wang, Y.; Li, G. Oxidative Capacity of Oxygen Nanobubbles and Their Mechanism for the Catalytic Oxidation of Ferrous Ions with Copper as a Catalyst in Sulfuric Acid Medium. *Langmuir* **2023**, *39* (29), 10112–10121.

(71) Waters, S.; Hamilton, D.; Pan, G.; Michener, S.; Ogilvie, S. Oxygen Nanobubbles for Lake Restoration—Where Are We at? A Review of a New-Generation Approach to Managing Lake Eutrophication. *Water* **2022**, *14* (13), 1989.

(72) Wang, B.; Wang, L.; Cen, W.; Lyu, T.; Jarvis, P.; Zhang, Y.; Zhang, Y.; Han, Y.; Wang, L.; Pan, G.; et al. Exploring a Chemical Input Free Advanced Oxidation Process Based on Nanobubble Technology to Treat Organic Micropollutants. *Environ. Pollut.* **2024**, *340*, 122877.

(73) Atkinson, A. J.; Apul, O. G.; Schneider, O.; Garcia-Segura, S.; Westerhoff, P. Nanobubble Technologies Offer Opportunities to Improve Water Treatment. *Acc. Chem. Res.* **2019**, *52* (5), 1196–1205.

(74) Liu, S.; Oshita, S.; Kawabata, S.; Makino, Y.; Yoshimoto, T. Identification of ROS Produced by Nanobubbles and Their Positive and Negative Effects on Vegetable Seed Germination. *Langmuir* **2016**, *32* (43), 11295–11302.

(75) Wang, L.; Ali, J.; Wang, Z.; Oladoja, N. A.; Cheng, R.; Zhang, C.; Mailhot, G.; Pan, G. Oxygen Nanobubbles Enhanced Photo-degradation of Oxytetracycline Under Visible Light: Synergistic Effect and Mechanism. *Chem. Eng. J.* **2020**, *388*, 124227.

(76) Zhang, M.; Seddon, J. R. T.; Lemay, S. G. Nanoparticle-Nanobubble Interactions: Charge Inversion and Re-Entrant Condensation of Amidine Latex Nanoparticles Driven by Bulk Nanobubbles. *J. Colloid Interface Sci.* **2019**, *538*, 605−610.

(77) Alheshibri, M.; Al Baroot, A.; Shui, L.; Zhang, M. Nanobubbles and Nanoparticles. *Curr. Opin. Colloid Interface Sci.* **2021**, *55*, 101470.

(78) Wu, S.; Hu, H.; Lin, Y.; Zhang, J.; Hu, Y. H. Visible Light Photocatalytic Degradation of Tetracycline over TiO2. *Chem. Eng. J.* **2020**, *382*, 122842.

(79) Wu, S.; Li, X.; Tian, Y.; Lin, Y.; Hu, Y. H. Excellent Photocatalytic Degradation of Tetracycline over Black Anatase-TiO2 Under Visible Light. *Chem. Eng. J.* **2021**, *406*, 126747.